Supporting Information

Edington et al. 10.1073/pnas.1722042115

Frequency Assignment of EDTA Spectral Features

Electronic structure calculations were used to assign the absorption features of EDTA (Fig. 3). FTIR spectra of EDTA (Fig. 3) show that the 1,588 cm^{-1} asymmetric stretching absorption for Ca^{2+}–EDTA is blue-shifted (increased in frequency) to 1,600 cm^{-1} in Mg^{2+}–EDTA and red-shifted (decreased in frequency) to 1,586 cm^{-1} in Sr^{2+}–EDTA. For La^{3+}, Tb^{3+}, and Lu^{3+} adducts of EDTA, the asymmetric stretching absorption is shifted to 1,592 cm^{-1}, 1,604 cm^{-1}, and 1,610 cm^{-1}, respectively. Based on results from electronic structure calculations, we assign the primary band to a combination of two nearly degenerate modes with B_{3u} symmetry. The weak shoulder is a mode with A_g symmetry that is IR-active because of the slightly distorted structure of the bound EDTA molecule. Computations predict that the asymmetric stretching absorption will blue-shift as the ionic radius of the bound ion is decreased and as the charge of the bound ion is increased (Fig. 6). Detailed parameters and results are provided in Table S1. This prediction is in good qualitative agreement with the experimental results (Fig. 3).

Two-Dimensional IR Spectrometer

The 2D IR measurements were taken using a custom-built 2D IR spectrometer, which is illustrated schematically in Fig. S2. The 800-nm, 100-fs, 12-μJ, 1-kHz repetition rate output of a Coherent Astrella Ti:sapphire regenerative amplifier was used to produce horizontally polarized midinfrared pulses 100 fs in width and spectrally centered at 6.2 μm via optical parametric amplification in a Light Conversion TOPAS-Prime followed by difference frequency generation in a Light Conversion noncollinear difference frequency generator. The midinfrared pulses were split into excitation (~95% of original pulse, transmitted), detection (~2.5% of original pulse, reflected), and reference (~2.5% of original pulse, reflected) beams using an uncoated CaF_2 wedge. Excitation pulse pairs were generated using a PhaseTech QuickShape Ge-based pulse shaper (1, 2). A two-frame phase cycle was used to remove residual scatter, and data were collected with a rotating-frame frequency of 1,400 cm^{-1}. The excitation and detection pulses were temporally overlapped by adjusting the optical path of the detection pulse with an Aerotech ANT95-L series linear nanopositioning stage. The reference pulse is not overlapped with the other two pulses and arrives at the sample area ~5 ns before the pump pulse pair. The polarization of the detection and reference pulses was controlled using a half-wave plate. The excitation, detection, and reference pulses were spatially overlapped in the sample in pump-probe geometry using gold-coated parabolic mirrors. The detection and reference pulses were filtered by a wire grid polarizer (Optometrics) before being dispersed onto a Teledyne 128 pixel × 128 pixel IR camera with 40-μm pixel pitch by an Andor Shamrock spectrograph. The detection and reference pulses were aligned onto the IR camera such that the detection pulse fell on the upper 64 pixel rows and the reference pulse fell on the lower 64 pixel rows. Pixels in the reference and detection regions of the camera were vertically binned for a maximum bit depth of 20 bits. All spectrometer control and data collection was performed using software written in LabView. Data analysis and plotting were performed using MATLAB. All 2D IR data shown were collected in the all-parallel (ZZZZ) polarization condition with the reference pulse blocked such that only the detection pulse fell on the IR camera. The path of the midinfrared pulses was purged with −100 °F dew point dry air such that no water vapor absorption features were visible in the detection spectrum. A total of 3×10^6 laser shots were collected to produce each 2D IR spectrum for $t_2 = 150$ fs while a total of 5×10^6 laser shots were collected to produce each 2D IR spectrum for $t_2 = 500$ fs to compensate for lower signal at greater delays.

Two-Dimensional IR Data Collection and Analysis

The 2D IR data are presented as the difference between the excited and ground-state infrared absorption spectrum (Fig. S3). The absorption spectrum measured by the detection pulse ($\omega_{detection}$) is plotted along the ordinate as a function of the excitation pulse frequency ($\omega_{excitation}$), which is plotted along the abscissa. Recall that 2D IR spectroscopy (*Two-Dimensional IR Spectrometer* and Fig. S2) uses both an excitation pulse (which interacts with the sample first) and detection pulse (which interacts with the sample second). The delay between excitation and detection pulses is labeled t_2, can be varied between 100 fs and several picoseconds, and is used to investigate vibrational relaxation and energy transfer processes.

Exciting the sample at a particular frequency will cause loss of absorption intensity at that frequency as the excitation pulse depopulates the vibrational ground state ("ground-state bleach") giving rise to the absorption (Fig. S3). This is accompanied by an increase in absorption at another, lower frequency due to absorption by the excited vibrational states populated by the excitation pulse ("excited state absorption"). Positive contours (colored in red) in the 2D IR surface denote a loss of intensity relative to the ground-state spectrum, while negative contours (colored in blue) indicate an increase in intensity relative to the ground-state spectrum. Regions of the spectrum unaffected by the pump pulse show zero intensity. In the data presented here, ground-state bleach features generally occur along or just above the diagonal, while excited state absorption features occur just below the diagonal.

Slices taken along the diagonal axis, where the excitation and detection pulses are the same frequency and ground-state bleaching is the dominant feature, are roughly equivalent to the conventional FTIR spectrum. Features which appear off the diagonal axis ("cross-peaks") reflect energy transfer between oscillators (3, 4). This occurs when two functional groups which absorb at different frequencies, e.g., a carbonyl and a carboxylate, are close enough to undergo rapid exchange of vibrational energy. Since the efficiency of vibrational energy transfer is sensitive to distance, cross-peaks can provide highly detailed, time-resolved molecular structure information (3, 4).

Calculation of CaM Binding Site Vibrational Relaxation

Since pump-probe signal in the carboxylate region (Fig. S5, 1,540 cm^{-1} to 1,590 cm^{-1}) partially overlaps the stronger amide I band (Fig. S5, 1,580 cm^{-1} to 1,650 cm^{-1}), vibrational relaxation parameters could not be extracted from carboxylate pump-probe decays. Instead, we employed an alternate approach to estimate vibrational relaxation in CaM's binding sites. We used pump-probe spectroscopy to measure vibrational relaxation in the amide I region, where signal is strong enough to extract accurate relaxation parameters from pump-probe data. The difference between maximum (S_{max}) and minimum (S_{min}) pump-probe amplitude at several waiting times between $t_2 = 300$ fs and $t_2 = 1{,}000$ fs was fit to a mono-exponential function of the form $S = Ae^{-kt}$. From these data, we were able to extract the decay constant k, describing the relaxation rate of the amide vibrational modes (Table S2).

We examined the 2D IR spectra and calculated r_1, the maximum amplitude of the carboxylate region divided by the maximum amplitude of the amide I region at $t_2 = 150$ fs, and r_2, the same ratio at 500 fs. We then calculated the ratio $R = r_2/r_1$, which provides a measure of how quickly the carboxylate region relaxes relative to the amide I region. Using R, the amide I decay

constant k_{AmI} extracted earlier from pump-probe spectroscopy, and $\Delta t = t_2 - t_1$, we estimated the carboxylate decay constant k_{COO-} using the relation $k_{COO-} = k_{AmI} - \ln(R)/\Delta t$, which is derived directly as a ratio of spectroscopic amplitudes, assuming that both the carboxylate and amide I regions of the spectrum obey monoexponential decay of the form $S = Ae^{-kt}$.

Estimation of Carboxylate Vibrational Coupling in CaM's Binding Sites

We used a simple transition dipole coupling model in combination with published structures of Ca^{2+}–CaM, our FTIR spectra of CaM, and estimates of Ln^{3+}-induced binding site contraction derived from our EDTA studies to calculate the likely extent of ion-dependent carboxylate vibrational coupling in the binding site.

We fit FTIR spectra of CaM to a sum of Gaussians of the following form:

$$\sum_n a_n e^{-\frac{\left(\nu-\nu_{0,n}\right)^2}{\sigma_n^2}}$$

where ν is the frequency of light in inverse centimeters, a_n is the peak experimental absorbance of feature n, $\nu_{0,n}$ is center frequency of the feature, and σ_n is related to the full width at half-maximum of the feature by

$$\mathrm{FWHM}_n = 2\sqrt{2ln(2)}\sigma_n.$$

Fits comprised two Gaussians: one for the amide I region and another for the carboxylate region. We used parameters derived from the carboxylate region fit for estimates of transition dipole strength. First, we calculated the carboxylate extinction coefficient as

$$\eta_n = \frac{a_n}{lC}$$

where η_n is the extinction coefficient (in molar per centimeter), a_n is the peak absorbance introduced earlier, l is the path length, and C is the sample concentration.

We used extinction coefficient, center frequency, and bandwidth parameters extracted from the fit to estimate the transition dipole of a typical carboxylate group in CaM's binding sites. We calculated the per-oscillator integrated absorption, A_n, as

$$A_n = \frac{\eta_n}{n_{osc}}\sqrt{2\pi}\sigma_n$$

where η_n is the extinction coefficient derived above, n_{osc} is the number of total carboxylate oscillators in the molecule (37), and σ_n is the Gaussian width parameter introduced earlier. This yields an estimate of $A_n = 2.9 \times 10^4\ \mathrm{M^{-1}\cdot cm^{-2}}$.

With an estimate of integrated absorption, it is possible to estimate the transition dipole, μ, as

$$|\mu|^2 = \frac{3\hbar nc\epsilon_0 ln10}{\pi\nu_{0,n}N_A}A_n$$

using a center frequency ν_0 of 1,560 $\mathrm{cm^{-1}}$; A_n as calculated before; $\hbar$, Planck's constant; c, the speed of light; ϵ_0, the permittivity of free space; and N_A, Avogadro's number; and converting to Debye, we thus estimate the carboxylate transition dipole to be at most 0.41 D. This is a conservative estimate for the following reasons: (*i*) The value of a_n used to derive A_n was the maximum carboxylate absorption observed (Ca^{2+}); μ increases with A_n; (*ii*) The value of σ_n was derived from the widest carboxylate absorption observed (apo); μ increases with σ_n; and (*iii*) The value of $\nu_{0,n}$ used the lowest reasonable frequency for a monodentate carboxylate (low-frequency edge of the monodentate Ln^{3+} carboxylate absorption); μ increases as $\nu_{0,n}$ decreases.

Since coupling increases with μ, these choices will yield an upper bound for the value of binding site coupling.

We next extracted the geometries of the carboxylate groups in each of calmodulin's four binding sites from a published structure of Ca^{2+}–CaM (PDB ID: 1CLM). Using these geometries in combination with the spectral estimate of the carboxylate transition dipole derived above, we calculated estimates of coupling between each carboxylate–carboxylate pair, $\beta_{i,j}$, in each binding site of apo-CaM using the relation below:

$$\beta_{i,j} = \frac{1}{4\pi\epsilon_0}\left[\frac{\vec{\boldsymbol{\mu}}_\mathbf{i}\cdot\vec{\boldsymbol{\mu}}_\mathbf{j}}{r_{i,j}^3} - 3\frac{\left(\vec{\boldsymbol{\mu}}_\mathbf{i}\cdot\vec{\mathbf{r}}_\mathbf{i,j}\right)\left(\vec{\boldsymbol{\mu}}_\mathbf{j}\cdot\vec{\mathbf{r}}_\mathbf{i,j}\right)}{r_{i,j}^5}\right]$$

where $\beta_{i,j}$ is the coupling between carboxylate groups i and j, $\boldsymbol{\mu}_\mathbf{i}$ and $\boldsymbol{\mu}_\mathbf{j}$ are the transition dipoles of carboxylate groups i and j, and $r_{i,j}$ is the distance between the central carbon atoms of the two carboxylate groups. Estimated couplings are tabulated in Table S3.

Since performing electronic structure modeling of even simplified Ln^{3+}-bound CaM binding sites proved prohibitive, we estimated the greatest likely binding site contraction present in Ln^{3+}-CaM using the results of our EDTA electronic structure calculations. Table S1 shows that the greatest degree of binding site contraction is observed in Lu^{3+}–EDTA, where the average oxygen ion coordination radius is 217 pm. Comparing this with the average oxygen ion coordination radius in Ca^{2+}–EDTA (233 pm), we observe an oxygen ion radius contraction of 16 pm. Since this contraction occurs on both sides of the bound ion, we can estimate that the total $Ca^{2+} \rightarrow Lu^{3+}$ binding site contraction is 32 pm.

To estimate coupling in the contracted binding site configurations, we uniformly decreased the values of $r_{i,j}$ extracted from the Ca^{2+}–CaM structure above by 32 pm and repeated the coupling calculations (Table S3). This method of estimating site contraction maximizes the value of $\beta_{i,j}$ since an $r_{i,j}$ contraction of 32 pm would only occur for coupling pairs that face each other directly through the bound ion. All other configurations would yield smaller contractions.

Even with the conservative assumptions detailed above, only 5 of the 18 total couplings are greater than 5 $\mathrm{cm^{-1}}$ in the contracted case. Couplings in the native Ca^{2+}–CaM case are uniformly smaller. We conclude that coupling does not have a significant effect on our results.

Vibrational Assignments of Ca^{2+}–CaM Binding Site Residues

To estimate the frequency shifts induced by Ca^{2+} within each binding pocket, we performed DFT frequency calculations using the Becke–Perdew 1986 functionals (5, 6) in combination with the Stuttgart/Dresden–Dunning basis set (7) (BP86/SDD). This is the same level of theory as used for EDTA above. In brief, starting with the crystal structure (PDB ID: 1CLM), we pruned each binding site by deleting all atoms except the two carbon atoms closest to the functional group of interest. The geometries of the sites used for frequency analyses are shown in Fig. 2. Next, we added missing hydrogens using the h_add command in pymol. All hydrogens were then relaxed at the BP86/SDD level by performing a geometry optimization while fixing the coordinates of all heavy atoms. These geometries were used as the starting point for performing further optimization and vibrational analysis of the individual ligands.

The optimizations were performed as follows: In each site, the ligand of interest was optimized while keeping all of the other ligands frozen. To preserve the distances and orientations of the crystal structures, the optimizations were performed in a series of four steps. First, the ligand is optimized while fixing the coordinates

of the oxygen and nitrogen atoms (amides) or two oxygen atoms (carboxylates), while relaxing the positions of all other atoms within the ligand. Next, the methyl groups hydrogens are fixed, and the remaining atoms are optimized. Finally, the cycle is repeated once again to ensure proper geometry convergence. Overall, this results in an energy-minimized geometry that maintains the position and orientation dictated by the initial crystal structure. In each site, the procedure is repeated for each of the five ligands of interest. Next, we perform a vibrational analysis on that ligand by diagonalizing the partial Hessian matrix involving the atoms corresponding to each specific ligand. This approach assumes negligible vibrational coupling between ligands. This is a good approximation, as coupling between sites is small, as evidenced by the small splitting. Deuterium masses were used for polar hydrogens in the vibrational analysis. Electronic structure calculations were performed using the Gaussian09 program and Hessian matrix analysis, and vibrational model assignments were done using MATLAB R2015a. The frequencies are tabulated in Table S4.

The electronic structure calculations show that monodentate carboxylates can vary significantly in frequency from 1,488 cm^{-1} to 1,529 cm^{-1}. If we apply the 43 cm^{-1} shift that we observe for EDTA (Fig. 3), the expected monodentate frequencies would fall within the 1,531 cm^{-1} to 1,572 cm^{-1} range, well within the observed side-chain frequencies observed in the FTIR and 2D IR spectra (Figs. 4 and 5). Bidentate carboxylates appear in the 1,481 cm^{-1} to 1,506 cm^{-1} range, ~40 cm^{-1} red-shifted, which agrees well with the difference between monodentate and bidentate peaks observed in the FTIR spectra (1,553 cm^{-1} bidentate, 1,580 cm^{-1} monodentate).

Similarly, we can assign the backbone amide frequencies (Table S4, ligand 2), which range from 1,600 cm^{-1} to 1,640 cm^{-1}; applying a similar ~43 cm^{-1} shift would put these modes squarely in the middle of the amide I band. It is important to note that, despite the positively charged Ca^{2+} ion, the amide residues are not strongly red-shifted, as would be expected for a strong electrostatic interaction between the C=O bond and a cation. Perhaps this is due to the electron-rich environment surrounding the ion. Sites 1 and 4 have a net −1 charge, whereas sites 2 and 3 have a net −2 charge. Thus, the negative charges from surrounding ligands cancel out the positive ion charge. Indeed, comparing the ligand 2 amide I frequencies with those of a single *N*-methylacetamide molecule computed at the same level of theory suggests a slight red-shift in sites 1 and 4, and a slight blue-shift in the remaining two. In conclusion, we expect the backbone C=Os involved in ligand binding to appear near the center of the amid I band. A similar analysis reveals that the asparagine side-chain vibrations (Sites 1, 4; ligand 6) will appear in the ~1,620 cm^{-1} to 1,630 cm^{-1} region. In conclusion, the cross-peaks observed in the 2D IR spectra (Fig. 5 and Table 2) are likely due to the ligands in the binding site. The ω_1 = ~1,593 cm^{-1} to 1,597 cm^{-1} excitation is likely due to monodentate carboxylates, whereas the ω_1 = ~1,613 cm^{-1} to 1,614 cm^{-1} is due to the asparagines. Detection ω_3 = ~1,633 cm^{-1} to 1,643 cm^{-1} is due to the backbone amide I modes within the binding site.

Computational Methods

All structures were based on a structure of EDTA coordinated to Ca^{2+} downloaded from the Cambridge Structural Database (CID 6049). For EDTA bound to ions other than Ca^{2+}, the original structure was modified by replacing Ca^{2+} with Mg^{2+}, Sr^{2+}, La^{3+}, Tb^{3+}, or Lu^{3+} before geometry optimization. All structures underwent full geometric optimization before computation of vibrational normal modes. Geometry optimization and computation were conducted at the BP86/SDD level of theory (5–10) using the Gaussian09 software (11). The Tb^{3+} geometry optimization was carried out using a quadratically convergent self-consistent field procedure because the high-spin complex was difficult to converge using the standard energy-direct inversion iterative subspace (EDIIS) procedure (12). All other optimizations were carried out using the standard EDIIS procedure.

1. Shim S-H, Strasfeld DB, Ling YL, Zanni MT (2007) Automated 2D IR spectroscopy using a mid-IR pulse shaper and application of this technology to the human islet amyloid polypeptide. *Proc Natl Acad Sci USA* 104:14197–14202.
2. Shim S-H, Zanni MT (2009) How to turn your pump-probe instrument into a multidimensional spectrometer: 2D IR and Vis spectroscopies via pulse shaping. *Phys Chem Chem Phys* 11:748–761.
3. Cho M (2009) *Two-Dimensional Optical Spectroscopy*, ed Cho M (Taylor Francis, New York).
4. Hamm P, Zanni M (2011) *Concepts and Methods of 2D Infrared Spectroscopy*, eds Hamm P, Zanni M (Cambridge Univ Press, New York).
5. Perdew JP (1986) Density-functional approximation for the correlation energy of the inhomogeneous electron gas. *Phys Rev B Condens Matter* 33:8822–8824.
6. Becke AD (1988) Density-functional exchange-energy approximation with correct asymptotic behavior. *Phys Rev A Gen Phys* 38:3098–3100.
7. Dunning TH, Jr, Hay PJ (1977) Gaussian basis sets for molecular calculations. *Methods of Electronic Structure Theory*, ed Schaefer HF (Springer, New York), pp 1–27.
8. Dolg M, Wedig U, Stoll H, Preuss H (1987) Energy-adjusted ab initio pseudopotentials for the first row transition elements. *J Chem Phys* 86:866–872.
9. Dolg M, Stoll H, Preuss H (1989) Energy-adjusted ab initio pseudopotentials for the rare earth elements. *J Chem Phys* 90:1730–1734.
10. Dolg M, Stoll H, Savin A, Preuss H (1989) Energy-adjusted pseudopotentials for the rare earth elements. *Theor Chim Acta* 75:173–194.
11. Frisch MJ, et al. (2009) Gaussian 09 Revision E.01 (Gaussian, Wallingford, CT).
12. Kudin KN, Scuseria GE, Cancès E (2002) A black-box self-consistent field convergence algorithm: One step closer. *J Chem Phys* 116:8255–8261.

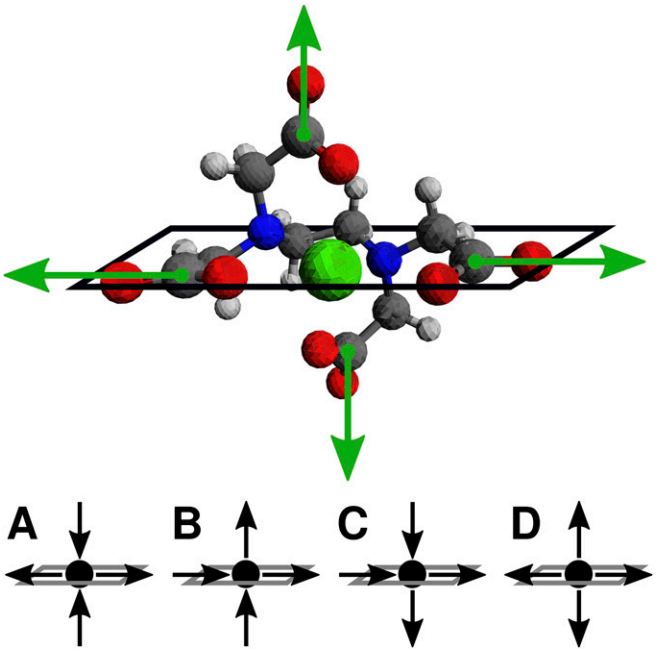

Fig. S1. (*Top*) Schematic of EDTA molecular structure bound to Ca^{2+} ion. (*Bottom*) Calculated vibrational modes of different symmetries are highlighted: A_g (*A*), B_u (*B*), B_u (*C*), and A_g (*D*). Note that modes *B* and *C* share B_u symmetry but are distinct.

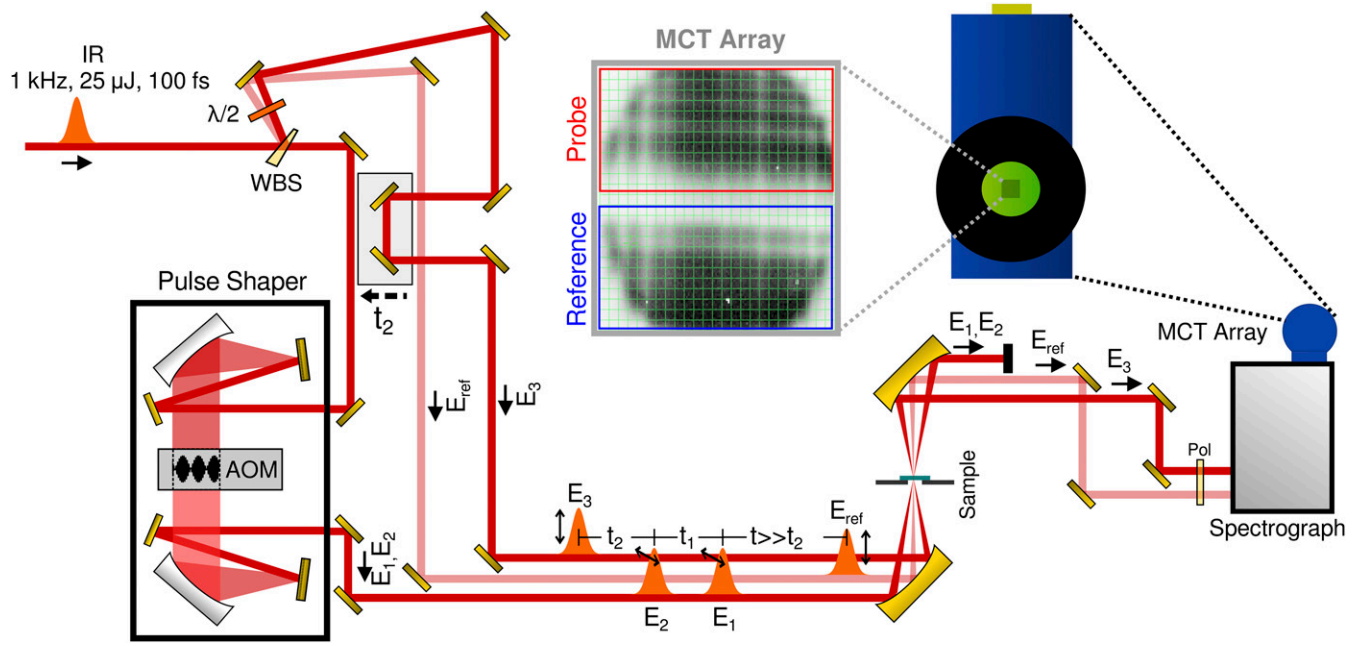

Fig. S2. Schematic of 2D IR spectrometer. AOM, acousto-optic modulator; E_1, first excitation pulse; E_2, second excitation pulse; E_3, detection pulse; E_{ref}, reference pulse; MCT, mercury cadmium telluride; t_2, excitation-detection delay; WBS, wedge beam splitter; and λ/2, half-wave plate. Direction of pulse propagation is denoted by single-headed arrows. Pulse polarization is denoted by double-headed arrows.

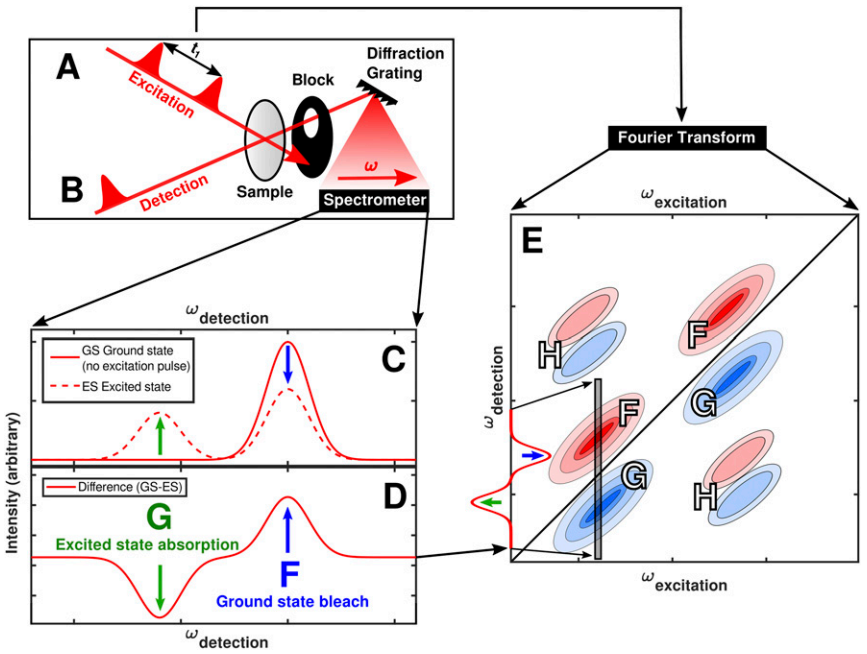

Fig. S3. Schematic of 2D IR spectroscopic setup. An excitation pulse, *A*, excites a sample before interrogation by a detection pulse, *B*. Infrared spectra of both the ground and excited states, *C*, are measured by the detection pulse. For ground-state spectra, the detection pulse is blocked before the sample. The differences of the ground and excited state spectra, *D*, are plotted along the vertical axis of the 2D IR plot, *E*, as a function of the frequency of the excitation pulse, which is plotted along the horizontal axis. Ground-state bleach features, *F*, occur along the diagonal and result from depopulation of the vibrational ground state by the excitation pulse. Excited state absorption features, *G*, occur just below the diagonal and result from infrared absorption by excited states generated by the excitation pulse. Spectral features that occur off the diagonal, *H*, are termed cross-peaks and indicate energy transfer between functional groups that absorb at different frequencies.

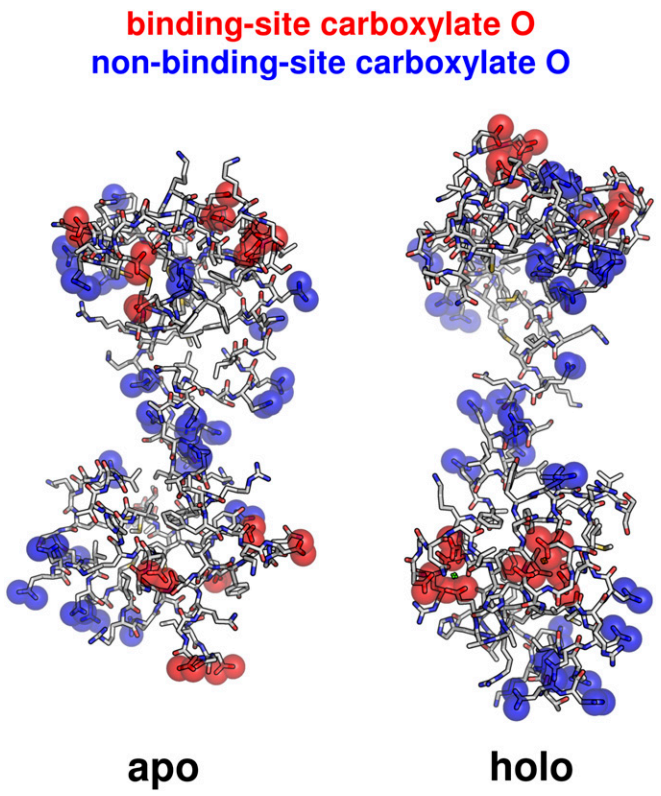

Fig. S4. Location of carboxylate oxygen atoms in both apo-CaM (PDB ID: 1DMO) and holo-CaM (PDB ID: 1CLM) structures. Carboxylates that participate in ion binding are colored red. Those that do not are colored blue. Ion binding induces a significant change in the environment of the binding site carboxylates, which cluster tightly around the ion. Little change is caused to the environment of the nonbinding carboxylates, which are always disperse and solvent-exposed.

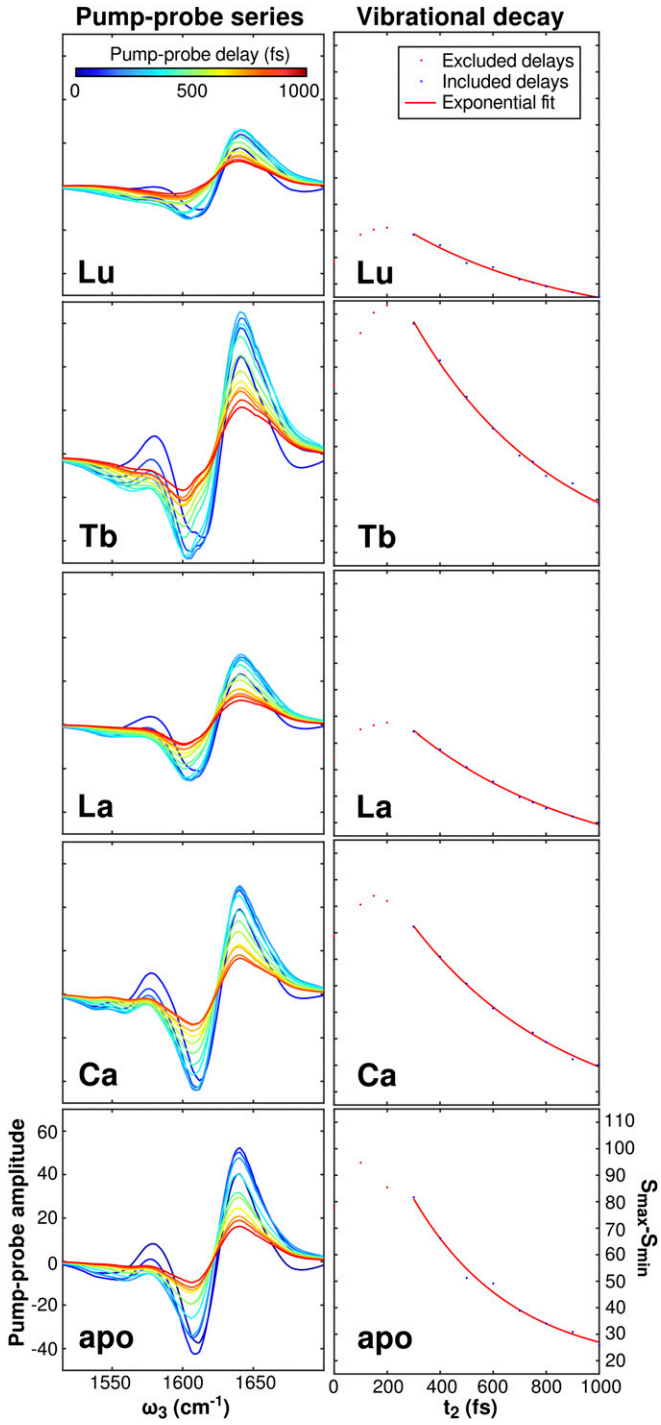

Fig. S5. Pump-probe measurements of CaM vibrational relaxation. (*Left*) Time-dependent pump-probe spectra of CaM bound to different ions. For each series, several spectra were taken at different t_2 delays between 0 fs and 1,000 fs. Spectra are not normalized. (*Right*) Monoexponential fits of each spectrum's decay. $S_{max} - S_{min}$ is calculated by subtracting the maximum pump-probe amplitude at a given time from the minimum pump-probe amplitude at that time. Fits are made to the t_2 interval 300 fs to 1,000 fs.

Table S1. Calculated absorption frequencies for the different EDTA vibrational modes A, B, C, and D shown in Fig. S1

Ion	r_i, pm	r_c, pm	A, cm^{-1}	B, cm^{-1}	C, cm^{-1}	D, cm^{-1}	$\upsilon_{principal}$, cm^{-1}	$\upsilon_{shoulder}$, cm^{-1}
Mg^{2+}	72	211	1,551	1,557	1,561	1,579	1,600	1,628
Ca^{2+}	99	233	1,538	1,542	1,545	1,563	1,588	1,612
Sr^{2+}	112	248	1,535	1,538	1,540	1,558	1,585	1,608
La^{3+}	106	235	1,570	1,573	1,574	1,593	1,592	1,625
Tb^{3+}	92	223	1,576	1,579	1,580	1,599	1,604	1,634
Lu^{3+}	85	217	1,583	1,586	1,588	1,608	1,608	1,638

Experimental absorption frequencies (Fig. 3) for the principal peak, $\upsilon_{principal}$, and the shoulder, $\upsilon_{shoulder}$, are included in the rightmost columns. Oxygen–metal coordination radii r_c are derived from DFT calculations and taken as the average of all four oxygen–metal radii for the given structure. Six-coordinate ionic radii r_i are included for comparison between ions.

Table S2. Vibrational relaxation parameters extracted from a combination of pump-probe and 2D IR spectra (Fig. 5 and Fig. S5)

Sample	r_1, t_2 = 150 fs (S_{COO-}/S_{AmI})	r_2, t_2 = 500 fs (S_{COO-}/S_{AmI})	R (r_2/r_1)	k_{AmI}, $fs^{-1} \times 10^3$	τ_{AmI}, fs	k_{COO-}, $fs^{-1} \times 10^3$	τ_{COO-}, fs
apo	0.17	0.069	0.41	1.7	590	4.3	230
Ca^{2+}	0.15	0.095	0.63	1.5	670	2.8	360
La^{3+}	0.19	0.079	0.42	1.5	670	4.0	250
Tb^{3+}	0.25	0.13	0.52	1.5	670	3.4	300

An abbreviated version of this table is included in the main text (Table 1); k_{AmI}, the decay constant for the amide I region extracted from a monoexponential fit to pump-probe measurements; k_{COO-}, the decay constant for the amide I region calculated from R and k_{AmI}; R, the ratio r_2/r_1; r_1, the ratio between the peak amplitude of the carboxylate and amide I regions of the 2D IR spectrum at t_2 = 150 fs; r_2, the ratio between the peak amplitude of the carboxylate and amide I regions of the 2D IR spectrum at t_2 = 500 fs; τ_{AmI}, the time constant for the amide I region calculated from k_{AmI}; τ_{COO-}, the time constant for the carboxylate region calculated from k_{COO-}.

Table S3. Estimated carboxylate vibrational couplings

Coupling pair	$\beta_{i,j}$ (Ca^{2+}), cm^{-1}	$\beta_{i,j}$ (32 pm contraction), cm^{-1}
BS1: ASP20 → ASP22	−3.7	−4.4
BS1: ASP20 → ASP24	−0.36	−0.44
BS1: ASP20 → GLU31	−0.95	−1.2
BS1: ASP22 → ASP24	5.8	7.2
BS1: ASP22 → GLU31	4.0	5.0
BS1: ASP24 → GLU31	−0.66	−0.78
BS2: ASP56 → ASP58	−4.5	−5.4
BS2: ASP56 → GLU67	−0.33	−0.41
BS2: ASP58 → GLU67	1.8	2.2
BS3: ASP93 → ASP95	−4.4	−5.3
BS3: ASP93 → GLU104	0.28	0.34
BS3: ASP95 → GLU104	3.0	3.7
BS4: ASP129 → ASP131	−4.4	−5.3
BS4: ASP129 → ASP133	−3.0	−3.6
BS4: ASP129 → GLU140	1.6	1.9
BS4: ASP131 → ASP133	10	13
BS4: ASP131 → GLU140	0.43	0.53
BS4: ASP133 → GLU140	−1.0	−1.2

ASP, aspartate; BS1, CaM binding site 1; BS2, binding site 2; BS3, binding site 3; BS4, binding site 4; GLU, glutamate. Numbers following amino acid abbreviations denote position in the CaM residue sequence.

Table S4. Frequencies calculated for the C=O stretching vibrations in CaM's four binding sites in the presence of Ca^{2+}

Ligand	Description	Frequency, cm^{-1}
Site 1 (charge = −2)		
1	Water	
2	THR26(C=O, backbone)	1,640
3	ASP20(COO^-, mono)	1,521
4	ASP22(COO^-, mono)	1,507
5	GLU31(COO^-, bi)	1,504
6	ASP24(COO^-, mono)	1,494
Site 2 (charge = −1)		
1	Water	
2	THR62(C=O, backbone)	1,608
3	ASP56(COO^-, mono)	1,518
4	ASP58(COO^-, mono)	1,529
5	GLU67(COO^-, bi)	1,481
6	ASN60(C=O, side-chain)	1,595
Site 3 (charge = −1)		
1	Water	
2	TYR99(C=O, backbone)	1,600
3	ASP93(COO^-, mono)	1,522
4	ASP95(COO^-, mono)	1,506
5	GLU104(COO^-, bi)	1,488
6	ASN97(C=O, side-chain)	1,585
Site 4 (charge = −2)		
1	Water	
2	GLN135(C=O, backbone)	1,627
3	ASP129(COO^-, mono)	1,529
4	ASP131(COO^-, mono)	1,526
5	GLU140(COO^-, bi)	1,506
6	ASP133(COO^-, mono)	1,498
Single ligands		
N-methylacetamide (NMA)		1,609
propionate ($CH3CH2COO^-$)		1,541
propanamide [CH3CH2C=O(NH2)]		1,619

For carboxylates (denoted by COO^- in the table), frequencies correspond to the carboxylate asymmetric stretching mode. For the amide units (denoted by C=O in the table), frequencies correspond to the C=O stretching mode. bi, bidentate carboxylate configuration; mono, monodentate carboxylate configuration. The sites are shown in Fig. 2. The frequencies of single ligands, shown at bottom, were computed for comparison with binding site frequencies. The shown site charges were calculated as the sum of Ca^{2+} charge and carboxylate charge in each binding site.